A comprehensive model of the railway wheelset-track interaction in curves

Authors: José Martínez-Casas1, Egidio Di Gialleonardo[2], Stefano Bruni[2], Luis Baeza[1*]

Affiliation:

[1]Centro de Investigación en Tecnología de Vehículos, Universitat Politècnica de València, Camino de Vera s/n, 46022 Valencia, Spain

[2]Dipartimento di Meccanica, Politecnico di Milano, Via La Masa 1, 20156 Milano, Italy

* Corresponding author

E-mail corresponding author: *baeza@mcm.upv.es*

Abstract

Train-track interaction has been extensively studied in the lat 40 years at least, leading to modelling approaches that can deal satisfactorily with many dynamic problems arising at the wheel/rail interface. However, the available models are usually not considering specifically the running dynamics of the vehicle in a curve, whereas a number of train-track interaction phenomena are specific to curve negotiation.

Aim of this paper is to define a model for a flexible wheelset running on a flexible curved track. The main novelty of this work is the assumption of a trajectory coordinates set that permits to consider curved tracks. Small relative displacements between the trajectory frame and the solid are considered, and they are modelled through Eulerian modal coordinates. The wheelset model is coupled to a cyclic track model having constant curvature by means of a wheel/rail contact model which accounts for the actual geometry of the contacting profiles and for the non-linear relationship between creepages and creep forces.

The proposed model can be used to analyse a variety of dynamic problems for railway vehicles, including rail corrugation and wheel polygonalisation, squeal noise, numerical estimation of the wheelset service loads. In this paper, simulation results are presented for some selected running conditions to exemplify the application of the model to the study of realistic train-track interaction cases and to point out the importance of curve negotiation effects specifically addressed in the work.

Keywords

Flexible wheelset, flexible curved track, train-track interaction

1. INTRODUCTION

Train-track interaction consists of the coupled vibration of a railway vehicle or train set and of a flexible track, with coupling of the two sub-systems being provided by wheel-rail contact forces and excitation arising mainly from surface imperfections in the rails and wheels, such as rail roughness and wheel out-of-roundness. In some cases, large level of vibration and large dynamic fluctuations of the contact forces may take place, leading to unwanted phenomena such as high levels of noise and vibration [1], damage of the rolling surfaces in the form of corrugation [2] or rolling contact fatigue [3]. Furthermore, train-track interaction also leads to dynamic stresses in the track components and in the wheelsets, which need to be carefully considered in order to avoid failures due to metal fatigue.

For these reasons, a large effort has been spent over the last 40 years to define suitable models for studying train-track interaction. Early models were mostly based on the representation of the vehicle as a system formed by rigid bodies, possibly simplified to considering only the wheelset as a rigid mass resting on a Hertzian stiffness [4]. More recently, the need to widen the frequency range of analysis led to the incorporation of wheelset flexibility in the models, leading to more realistic representation of wheel-rail interaction effects at higher frequencies. For the study of rail corrugation and wheel polygonalisation, generally a modal synthesis is introduced to reduce the size of the problem [5 – 7], whereas in case the frequency range of interest up to 1kHz and above (such as for the study of rolling noise) a Finite Element model of the wheel or wheelset is used without condensation [8, 9]. Only very recently, a further model refinement was introduced to consider the inertial effects due to wheelset rotation [10, 11].

It should be noted that many phenomena related with train-track interaction, particularly squeal noise, short pitch rail corrugation and the largest stresses generated in the wheels and axle, are mostly occurring when the rail vehicle negotiates a curved track, calling for a proper consideration of the effects related with wheelset curving in train-track interaction models. When a rail vehicle runs through a curve, two mutually influencing phenomena take place at wheel rail contact: on one hand, contact parameters such as the contact point position, the normal and creep forces, creepages are slowly evolving in response to curve negotiation. On the other hand, the same quantities are subject to faster changes due to high-frequency interaction of the flexible bodies in contact. On account of the non-linearity of the problem, the two effects cannot be superimposed and a more comprehensive approach needs to be deployed which, to the Authors' knowledge, has not been presented yet.

The aim of this paper is therefore to propose a mathematical model for the dynamics of a flexible wheelset running through a curve and interacting with a flexible railway track, considering in full the non-linearities introduced by wheel-rail contact. In order to keep within reasonable limits the computational complexity of the problem, a trajectory coordinates set is introduced that permits to describe the large motion of the wheelset along the curved track, and the small relative movements of the wheelset with respect to the trajectory frame are described by means of Eulerian modal coordinates introduced with respect to a set of modal shapes obtained from a finite element model of the wheelset. The first 100 modes of vibration of the flexible wheelset are considered, covering a frequency range up to 2.7 kHz approximately. The wheelset model is coupled to a cyclic track model having constant curvature by means of a wheel/rail contact model which accounts for the actual geometry of the contacting profiles and for the non-linear relationship between creepages and creep forces.

Results for the proposed modelling approach are presented for a selected vehicle type and curving condition, and for different excitation sources including short wavelength geometric imperfections in the rail profiles and singularities such as wheel flats. Results are also presented for the wheelset running in tangent track, to point out the importance of curve negotiation effects specifically addressed in this work.

The paper is organised as follows: in Section 2 the equations of motion for the flexible wheelset in a curve are introduced. In Section 3 the model of a cyclic curved flexible track is presented. In Section 4 the model of wheel-rail contact forces is introduced and the final equations of the train-track interaction problem are derived. In Section 5 simulation results are presented for some selected running conditions and finally in Section 6 conclusive remark are provided.

2. THE FLEXIBLE WHEELSET MODEL IN CURVED TRACK

The study of vehicle-track interaction is carried out in this paper considering one single wheelset, given that in the frequency range of interest the dynamics of the sprung masses (bogie frame and car body) are effectively isolated from the motion of the un-sprung masses (wheelsets and axle boxes) on account of the mechanical filter introduced by the suspensions. The effect of low frequency curving dynamics of the complete vehicle needs however to be included in the model, in order to obtain suitable mean values for the creepages and contact forces, which affect the coupled wheelset-track vibration also at higher frequency. This is accomplished by prescribing the forces applied by the primary suspension to the wheelset in the vertical plane and the yaw displacement of the bogie at the primary suspension, as explained in Section 2.2.

2.1. Equations of motion of the flexible wheelset

In order to model the flexible wheelset travelling on curved track, two frames of reference are considered (see Fig. 1). The first one is an inertial frame $\mathbf{X}_0\mathbf{Y}_0\mathbf{Z}_0$ which is fixed in an arbitrary point. The second is a trajectory coordinate frame $\mathbf{X}_T\mathbf{Y}_T\mathbf{Z}_T$ that follows the motion of the wheelset. The system $\mathbf{X}_T\mathbf{Y}_T\mathbf{Z}_T$ is centred in the undeformed configuration of the wheelset, being the $\mathbf{X}_T$-axis parallel to the forward speed, the $\mathbf{Y}_T$-axis parallel to wheelset axis and the $\mathbf{Z}_T$-axis is vertically up. A vector referred to the fixed and trajectory frame is denoted by $\mathbf{a}_0$ and $\mathbf{a}$, respectively.

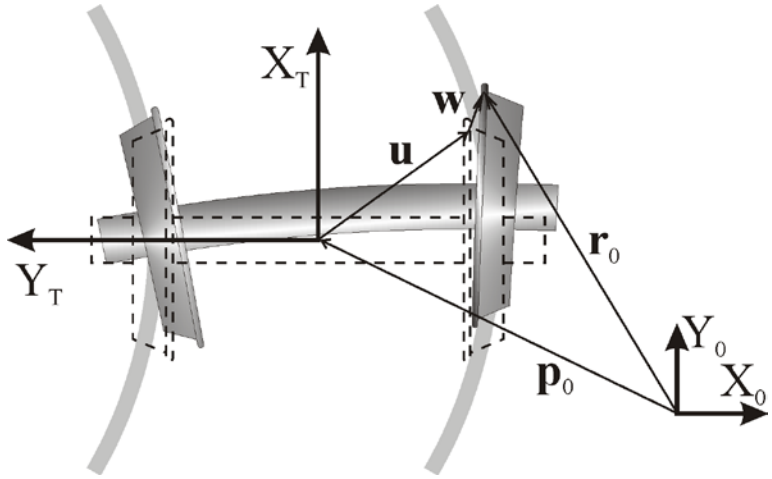

Figure 1: Frames of reference and position vectors. In dashed trace is shown the undeformed configuration of the wheelset. In solid colours is sketched a generic position of the flexible wheelset.

The coordinates that are implemented in the wheelset model do not follow the material points of the solid which is the commonest procedure in Mechanics, nonetheless they are associated with spatial points (Eulerian approach). The position vector $\mathbf{r}_0$ of a material particle which is in the spatial position $\mathbf{u}$ at instant t for the undeformed configuration, can be defined by means of the following formula:

$$\mathbf{r}_0 = \mathbf{p}_0 + \mathbf{T}\,(\mathbf{u} + \mathbf{w}(\mathbf{u}, t))\,, \tag{1}$$

where $\mathbf{p}_0$ is the position vector of the track frame; $\mathbf{w}$ corresponds to the displacement vector due to the elastic deformation and small rigid body displacement of the solid; $\mathbf{T}$ is the rotation matrix that relations the trajectory frame of the track with the fixed frame.

Considering that the coordinate frame is chosen so that the wheelset spin rotation Ω is in the second axle $\mathbf{Y}_T$, the angular velocity tensor $\widetilde{\mathbf{\Omega}}$ is defined as follows:

$$\widetilde{\mathbf{\Omega}} = \begin{bmatrix} 0 & 0 & \Omega \\ 0 & 0 & 0 \\ -\Omega & 0 & 0 \end{bmatrix} = \Omega\,\mathbf{J}\,; \text{ and } \mathbf{J} = \begin{bmatrix} 0 & 0 & 1 \\ 0 & 0 & 0 \\ -1 & 0 & 0 \end{bmatrix}. \tag{2}$$

The velocity due to the rigid body spinning is:

$$\mathbf{v} = \begin{pmatrix} v_1 & v_2 & v_3 \end{pmatrix}^{\mathrm{T}} = \widetilde{\mathbf{\Omega}}\,\mathbf{u} = \Omega\,\mathbf{J}\,\mathbf{u} = \Omega\,\widetilde{\mathbf{u}}\,, \tag{3}$$

where $\widetilde{\mathbf{u}} = \begin{pmatrix} u_3 & 0 & -u_1 \end{pmatrix}^{\mathrm{T}}$. The velocity of the particle is computed through the material derivative of $\mathbf{r}_0$, and in the trajectory frame that is:

$$\begin{aligned} \frac{\mathrm{D}\mathbf{r}}{\mathrm{D}t} &= \mathbf{T}^{\mathrm{T}}\,\dot{\mathbf{p}}_0 + \mathbf{T}^{\mathrm{T}}\,\dot{\mathbf{T}}\,(\mathbf{u} + \mathbf{w}) + \dot{\mathbf{w}} + \sum_i v_i \frac{\partial \mathbf{u}}{\partial u_i} + \sum_i v_i \frac{\partial \mathbf{w}}{\partial u_i} \\ &= \dot{\mathbf{p}} + \widetilde{\boldsymbol{\omega}}\,(\mathbf{u} + \mathbf{w}) + \dot{\mathbf{w}} + \Omega\,\mathbf{J}\,\mathbf{u} + \Omega \sum_i \widetilde{u}_i \frac{\partial \mathbf{w}}{\partial u_i} \end{aligned}\,, \tag{4}$$

being $\dot{\mathbf{p}}$ the speed of the track frame centre (expressed in the trajectory frame) and $\widetilde{\boldsymbol{\omega}} = \mathbf{T}^{\mathrm{T}}\,\dot{\mathbf{T}}$ the angular velocity matrix of the track frame. The two first velocity terms are associated to translational and rotational movement of the track frame, respectively; $\dot{\mathbf{w}}$ represents the velocity of the spatial point due to the flexibility; the term $\Omega\,\mathbf{J}\,\mathbf{u}$ is the velocity due to the rigid body spinning; and the last term is the convective velocity associated with the Eulerian coordinate system.

In order to obtain the expression of the kinetic energy for the wheelset, the square of the particle velocity is obtained, which reads:

$$\begin{aligned} \frac{\mathrm{D}\mathbf{r}^{\mathrm{T}}}{\mathrm{D}t}\frac{\mathrm{D}\mathbf{r}}{\mathrm{D}t} &= \dot{\mathbf{p}}^{\mathrm{T}}\,\dot{\mathbf{p}} + 2\,\dot{\mathbf{p}}^{\mathrm{T}}\,\widetilde{\boldsymbol{\omega}}\,(\mathbf{u} + \mathbf{w}) + 2\,\Omega\,\dot{\mathbf{p}}^{\mathrm{T}}\,\mathbf{J}\,\mathbf{u} + 2\,\dot{\mathbf{p}}^{\mathrm{T}}\,\dot{\mathbf{w}} + 2\,\Omega\,\dot{\mathbf{p}}^{\mathrm{T}}\left(\sum_i \widetilde{u}_i \frac{\partial \mathbf{w}}{\partial u_i}\right) \\ &+ \left(\mathbf{u}^{\mathrm{T}} + \mathbf{w}^{\mathrm{T}}\right)\widetilde{\boldsymbol{\omega}}^{\mathrm{T}}\,\widetilde{\boldsymbol{\omega}}\,(\mathbf{u} + \mathbf{w}) + 2\left(\mathbf{u}^{\mathrm{T}} + \mathbf{w}^{\mathrm{T}}\right)\widetilde{\boldsymbol{\omega}}^{\mathrm{T}}\,\dot{\mathbf{w}} + 2\,\Omega\left(\mathbf{u}^{\mathrm{T}} + \mathbf{w}^{\mathrm{T}}\right)\widetilde{\boldsymbol{\omega}}^{\mathrm{T}}\,\mathbf{J}\,\mathbf{u} \\ &+ 2\,\Omega\left(\sum_i \widetilde{u}_i \frac{\partial \mathbf{w}^{\mathrm{T}}}{\partial u_i}\right)\widetilde{\boldsymbol{\omega}}\,(\mathbf{u} + \mathbf{w}) + \dot{\mathbf{w}}^{\mathrm{T}}\,\dot{\mathbf{w}} + 2\,\Omega\,\dot{\mathbf{w}}^{\mathrm{T}}\,\mathbf{J}\,\mathbf{u} + 2\,\Omega\,\dot{\mathbf{w}}^{\mathrm{T}}\left(\sum_i \widetilde{u}_i \frac{\partial \mathbf{w}}{\partial u_i}\right) \cdot \\ &+ \Omega^2\,\mathbf{u}^{\mathrm{T}}\,\mathbf{J}^{\mathrm{T}}\,\mathbf{J}\,\mathbf{u} + 2\,\Omega^2\left(\sum_i \widetilde{u}_i \frac{\partial \mathbf{w}^{\mathrm{T}}}{\partial u_i}\right)\mathbf{J}\,\mathbf{u} + \Omega^2\left(\sum_i \widetilde{u}_i \frac{\partial \mathbf{w}^{\mathrm{T}}}{\partial u_i}\right)\left(\sum_i \widetilde{u}_i \frac{\partial \mathbf{w}}{\partial u_i}\right) \end{aligned} \tag{5}$$

Due to the geometry of revolution of the wheelset, the displacement vector $\mathbf{w}$ can be calculated through superposition of mode shapes in the non-rotating trayectory frame $\mathbf{X}_T\mathbf{Y}_T\mathbf{Z}_T$:

$$\mathbf{w}(\mathbf{u},t) = \mathbf{\Phi}(\mathbf{u})\,\mathbf{q}(t), \tag{6}$$

where $\mathbf{\Phi}(\mathbf{u})$ is the mode shape functions matrix of the free-boundary wheelset and $\mathbf{q}(t)$ is the Eulerian-modal coordinate vector. The small rigid body displacements of the solid are considered in this approach through the rigid body modes of the wheelset. It must be pointed out that the mode shape functions do not depend on time since the rotation of the solid does not change the mode shapes functions in spatial coordinates, because of the axial symmetry of the wheelset. Once the formula Eq. (6) is applied in Eq. (5), the kinetic energy results in the following expression:

$$\begin{aligned}
E_K = {} & \frac{1}{2}\int_{vol} \frac{\mathrm{D}\mathbf{r}^{\mathrm{T}}}{\mathrm{D}t}\frac{\mathrm{D}\mathbf{r}}{\mathrm{D}t}\rho\,\mathrm{d}v = \frac{1}{2}\dot{\mathbf{p}}^{\mathrm{T}}\dot{\mathbf{p}}\,m_w + \dot{\mathbf{p}}^{\mathrm{T}}\tilde{\boldsymbol{\omega}}\int_{vol}\rho\,\mathbf{u}\,\mathrm{d}v + \dot{\mathbf{p}}^{\mathrm{T}}\tilde{\boldsymbol{\omega}}\int_{vol}\rho\mathbf{\Phi}\,\mathrm{d}v\,\mathbf{q} + \Omega\,\dot{\mathbf{p}}^{\mathrm{T}}\mathbf{J}\int_{vol}\rho\,\mathbf{u}\,\mathrm{d}v \\
& + \dot{\mathbf{p}}^{\mathrm{T}}\int_{vol}\rho\mathbf{\Phi}\,\mathrm{d}v\,\dot{\mathbf{q}} + \Omega\,\dot{\mathbf{p}}^{\mathrm{T}}\int_{vol}\rho\left(\sum_i \tilde{u}_i\frac{\partial\mathbf{\Phi}}{\partial u_i}\right)\mathrm{d}v\,\mathbf{q} + \frac{1}{2}\int_{vol}\rho\,\mathbf{u}^{\mathrm{T}}\tilde{\boldsymbol{\omega}}^{\mathrm{T}}\tilde{\boldsymbol{\omega}}\,\mathbf{u}\,\mathrm{d}v \\
& + \int_{vol}\rho\,\mathbf{u}^{\mathrm{T}}\tilde{\boldsymbol{\omega}}^{\mathrm{T}}\tilde{\boldsymbol{\omega}}\mathbf{\Phi}\,\mathrm{d}v\,\mathbf{q} + \frac{1}{2}\mathbf{q}^{\mathrm{T}}\int_{vol}\rho\mathbf{\Phi}^{\mathrm{T}}\tilde{\boldsymbol{\omega}}^{\mathrm{T}}\tilde{\boldsymbol{\omega}}\mathbf{\Phi}\,\mathrm{d}v\,\mathbf{q} + \int_{vol}\rho\,\mathbf{u}^{\mathrm{T}}\tilde{\boldsymbol{\omega}}^{\mathrm{T}}\mathbf{\Phi}\,\mathrm{d}v\,\dot{\mathbf{q}} \\
& + \mathbf{q}^{\mathrm{T}}\int_{vol}\rho\mathbf{\Phi}^{\mathrm{T}}\tilde{\boldsymbol{\omega}}^{\mathrm{T}}\mathbf{\Phi}\,\mathrm{d}v\,\dot{\mathbf{q}} + \Omega\int_{vol}\rho\,\mathbf{u}^{\mathrm{T}}\tilde{\boldsymbol{\omega}}^{\mathrm{T}}\mathbf{J}\,\mathbf{u}\,\mathrm{d}v + \Omega\,\mathbf{q}^{\mathrm{T}}\int_{vol}\rho\mathbf{\Phi}^{\mathrm{T}}\tilde{\boldsymbol{\omega}}^{\mathrm{T}}\mathbf{J}\,\mathbf{u}\,\mathrm{d}v \\
& + \Omega\,\mathbf{q}^{\mathrm{T}}\int_{vol}\rho\left(\sum_i \tilde{u}_i\frac{\partial\mathbf{\Phi}^{\mathrm{T}}}{\partial u_i}\right)\tilde{\boldsymbol{\omega}}\,\mathbf{u}\,\mathrm{d}v + \Omega\,\mathbf{q}^{\mathrm{T}}\int_{vol}\rho\left(\sum_i \tilde{u}_i\frac{\partial\mathbf{\Phi}^{\mathrm{T}}}{\partial u_i}\right)\tilde{\boldsymbol{\omega}}\mathbf{\Phi}\,\mathrm{d}v\,\mathbf{q} \\
& + \frac{1}{2}\dot{\mathbf{q}}^{\mathrm{T}}\dot{\mathbf{q}} + \Omega\,\dot{\mathbf{q}}^{\mathrm{T}}\int_{vol}\rho\mathbf{\Phi}^{\mathrm{T}}\mathbf{J}\,\mathbf{u}\,\mathrm{d}v + \Omega\,\dot{\mathbf{q}}^{\mathrm{T}}\int_{vol}\rho\mathbf{\Phi}^{\mathrm{T}}\left(\sum_i \tilde{u}_i\frac{\partial\mathbf{\Phi}}{\partial u_i}\right)\mathrm{d}v\,\mathbf{q} \\
& + \frac{1}{2}\Omega^2\int_{vol}\rho\,\mathbf{u}^{\mathrm{T}}\mathbf{E}\,\mathbf{u}\,\mathrm{d}v + \Omega^2\,\mathbf{q}^{\mathrm{T}}\int_{vol}\rho\left(\sum_i \tilde{u}_i\frac{\partial\mathbf{\Phi}^{\mathrm{T}}}{\partial u_i}\right)\mathbf{J}\,\mathbf{u}\,\mathrm{d}v \\
& + \frac{1}{2}\Omega^2\,\mathbf{q}^{\mathrm{T}}\int_{vol}\rho\left(\sum_i \tilde{u}_i\frac{\partial\mathbf{\Phi}^{\mathrm{T}}}{\partial u_i}\right)\left(\sum_i \tilde{u}_i\frac{\partial\mathbf{\Phi}}{\partial u_i}\right)\mathrm{d}v\,\mathbf{q}
\end{aligned} \quad . \tag{7}$$

Once the kinetic energy is known, the two terms of Lagrange's equation are computed as follows:

$$\begin{aligned}
\left(\frac{\partial E_K}{\partial\mathbf{q}}\right)^{\mathrm{T}} = {} & \int_{vol}\rho\mathbf{\Phi}^{\mathrm{T}}\,\mathrm{d}v\,\tilde{\boldsymbol{\omega}}^{\mathrm{T}}\dot{\mathbf{p}} + \Omega\int_{vol}\rho\left(\sum_i \tilde{u}_i\frac{\partial\mathbf{\Phi}^{\mathrm{T}}}{\partial u_i}\right)\mathrm{d}v\,\dot{\mathbf{p}} + \int_{vol}\rho\mathbf{\Phi}^{\mathrm{T}}\tilde{\boldsymbol{\omega}}^{\mathrm{T}}\tilde{\boldsymbol{\omega}}\,\mathbf{u}\,\mathrm{d}v \\
& + \int_{vol}\rho\mathbf{\Phi}^{\mathrm{T}}\tilde{\boldsymbol{\omega}}^{\mathrm{T}}\tilde{\boldsymbol{\omega}}\mathbf{\Phi}\,\mathrm{d}v\,\mathbf{q} + \int_{vol}\rho\mathbf{\Phi}^{\mathrm{T}}\tilde{\boldsymbol{\omega}}^{\mathrm{T}}\mathbf{\Phi}\,\mathrm{d}v\,\dot{\mathbf{q}} + \Omega\int_{vol}\rho\mathbf{\Phi}^{\mathrm{T}}\tilde{\boldsymbol{\omega}}^{\mathrm{T}}\mathbf{J}\,\mathbf{u}\,\mathrm{d}v \\
& + \Omega\int_{vol}\rho\left(\sum_i \tilde{u}_i\frac{\partial\mathbf{\Phi}^{\mathrm{T}}}{\partial u_i}\right)\tilde{\boldsymbol{\omega}}\,\mathbf{u}\,\mathrm{d}v + \Omega\int_{vol}\rho\left(\sum_i \tilde{u}_i\frac{\partial\mathbf{\Phi}^{\mathrm{T}}}{\partial u_i}\right)\tilde{\boldsymbol{\omega}}\mathbf{\Phi}\,\mathrm{d}v\,\mathbf{q} \\
& + \Omega\int_{vol}\rho\mathbf{\Phi}^{\mathrm{T}}\tilde{\boldsymbol{\omega}}^{\mathrm{T}}\left(\sum_i \tilde{u}_i\frac{\partial\mathbf{\Phi}}{\partial u_i}\right)\mathrm{d}v\,\mathbf{q} + \Omega\int_{vol}\rho\left(\sum_i \tilde{u}_i\frac{\partial\mathbf{\Phi}^{\mathrm{T}}}{\partial u_i}\right)\mathbf{\Phi}\,\mathrm{d}v\,\dot{\mathbf{q}} \\
& + \Omega^2\int_{vol}\rho\left(\sum_i \tilde{u}_i\frac{\partial\mathbf{\Phi}^{\mathrm{T}}}{\partial u_i}\right)\mathbf{J}\,\mathbf{u}\,\mathrm{d}v + \Omega^2\int_{vol}\rho\left(\sum_i \tilde{u}_i\frac{\partial\mathbf{\Phi}^{\mathrm{T}}}{\partial u_i}\right)\left(\sum_i \tilde{u}_i\frac{\partial\mathbf{\Phi}}{\partial u_i}\right)\mathrm{d}v\,\mathbf{q}
\end{aligned} \quad , \tag{8}$$

$$\frac{\mathrm{D}}{\mathrm{D}t}\left(\frac{\partial E_K}{\partial \dot{\mathbf{q}}}\right)^{\mathrm{T}} = \int_{vol}\rho\boldsymbol{\Phi}^{\mathrm{T}}\,\mathrm{d}v\,\ddot{\mathbf{p}} + \int_{vol}\rho\boldsymbol{\Phi}^{\mathrm{T}}\,\tilde{\dot{\boldsymbol{\omega}}}\,\mathbf{u}\,\mathrm{d}v + \int_{vol}\rho\boldsymbol{\Phi}^{\mathrm{T}}\,\tilde{\dot{\boldsymbol{\omega}}}\,\boldsymbol{\Phi}\,\mathrm{d}v\,\mathbf{q} + \int_{vol}\rho\boldsymbol{\Phi}^{\mathrm{T}}\,\tilde{\boldsymbol{\omega}}\,\boldsymbol{\Phi}\,\mathrm{d}v\,\dot{\mathbf{q}}$$
$$+\ddot{\mathbf{q}} + \Omega\int_{vol}\rho\boldsymbol{\Phi}^{\mathrm{T}}\left(\sum_i \tilde{u}_i\frac{\partial\boldsymbol{\Phi}}{\partial u_i}\right)\mathrm{d}v\,\dot{\mathbf{q}} + \Omega\int_{vol}\rho\left(\sum_i \tilde{u}_i\frac{\partial\boldsymbol{\Phi}^{\mathrm{T}}}{\partial u_i}\right)\mathrm{d}v\,\dot{\mathbf{p}}$$
$$+\Omega\int_{vol}\rho\left(\sum_i \tilde{u}_i\frac{\partial\boldsymbol{\Phi}^{\mathrm{T}}}{\partial u_i}\right)\tilde{\boldsymbol{\omega}}\,\mathbf{u}\,\mathrm{d}v + \Omega\int_{vol}\rho\boldsymbol{\Phi}^{\mathrm{T}}\,\tilde{\boldsymbol{\omega}}\,\mathbf{J}\,\mathbf{u}\,\mathrm{d}v$$
$$+\Omega\int_{vol}\rho\left(\sum_i \tilde{u}_i\frac{\partial\boldsymbol{\Phi}^{\mathrm{T}}}{\partial u_i}\right)\tilde{\boldsymbol{\omega}}\,\boldsymbol{\Phi}\,\mathrm{d}v\,\mathbf{q} + \Omega\int_{vol}\rho\boldsymbol{\Phi}^{\mathrm{T}}\,\tilde{\boldsymbol{\omega}}\left(\sum_i \tilde{u}_i\frac{\partial\boldsymbol{\Phi}}{\partial u_i}\right)\mathrm{d}v\,\mathbf{q}$$
$$+\Omega^2\int_{vol}\rho\left(\sum_i \tilde{u}_i\frac{\partial\boldsymbol{\Phi}^{\mathrm{T}}}{\partial u_i}\right)\mathbf{J}\,\mathbf{u}\,\mathrm{d}v - \Omega^2\int_{vol}\rho\boldsymbol{\Phi}^{\mathrm{T}}\,\mathbf{E}\,\mathbf{u}\,\mathrm{d}v$$
$$+\Omega^2\int_{vol}\rho\left(\sum_i \tilde{u}_i\frac{\partial\boldsymbol{\Phi}^{\mathrm{T}}}{\partial u_i}\right)\left(\sum_i \tilde{u}_i\frac{\partial\boldsymbol{\Phi}}{\partial u_i}\right)\mathrm{d}v\,\mathbf{q} - \Omega^2\int_{vol}\rho\boldsymbol{\Phi}^{\mathrm{T}}\left(\sum_{i=1,3} u_i\frac{\partial\boldsymbol{\Phi}}{\partial u_i}\right)\mathrm{d}v\,\mathbf{q}$$
$$+\Omega^2\int_{vol}\rho\boldsymbol{\Phi}^{\mathrm{T}}\left(\sum_i\sum_j \tilde{u}_i\,\tilde{u}_j\frac{\partial^2\boldsymbol{\Phi}}{\partial u_i\,\partial u_j}\right)\mathrm{d}v\,\mathbf{q} \quad , \tag{9}$$

being $\mathbf{E} = -\mathbf{J}\,\mathbf{J} = \begin{bmatrix}1 & 0 & 0\\ 0 & 0 & 0\\ 0 & 0 & 1\end{bmatrix}$.

The equation of motion of the flexible and rotating wheelset is derived by means of Lagrange's equation. Considering Eqs. (8) and (9) and taking into account that matrix $\tilde{\boldsymbol{\omega}}$ is anti-symmetric, the following equation is obtained:

$$\ddot{\mathbf{q}} + \left[2\Omega\int_{vol}\rho\boldsymbol{\Phi}^{\mathrm{T}}\left(\sum_i \tilde{u}_i\frac{\partial\boldsymbol{\Phi}}{\partial u_i}\right)\mathrm{d}v + 2\int_{vol}\rho\boldsymbol{\Phi}^{\mathrm{T}}\,\tilde{\boldsymbol{\omega}}\,\boldsymbol{\Phi}\,\mathrm{d}v\right]\dot{\mathbf{q}}$$
$$+\left[\Omega^2\int_{vol}\rho\boldsymbol{\Phi}^{\mathrm{T}}\left(\sum_i\sum_j \tilde{u}_i\,\tilde{u}_j\frac{\partial^2\boldsymbol{\Phi}}{\partial u_i\,\partial u_j}\right)\mathrm{d}v - \Omega^2\int_{vol}\rho\boldsymbol{\Phi}^{\mathrm{T}}\left(\sum_{i=1,3} u_i\frac{\partial\boldsymbol{\Phi}}{\partial u_i}\right)\mathrm{d}v\right.$$
$$\left.+2\Omega\int_{vol}\rho\boldsymbol{\Phi}^{\mathrm{T}}\,\tilde{\boldsymbol{\omega}}\left(\sum_i \tilde{u}_i\frac{\partial\boldsymbol{\Phi}}{\partial u_i}\right)\mathrm{d}v + \int_{vol}\rho\boldsymbol{\Phi}^{\mathrm{T}}\,\tilde{\dot{\boldsymbol{\omega}}}\,\boldsymbol{\Phi}\,\mathrm{d}v - \int_{vol}\rho\boldsymbol{\Phi}^{\mathrm{T}}\,\tilde{\boldsymbol{\omega}}^{\mathrm{T}}\,\tilde{\boldsymbol{\omega}}\,\boldsymbol{\Phi}\,\mathrm{d}v\right]\mathbf{q}. \tag{10}$$
$$= \Omega^2\int_{vol}\rho\boldsymbol{\Phi}^{\mathrm{T}}\,\mathbf{E}\,\mathbf{u}\,\mathrm{d}v - 2\Omega\int_{vol}\rho\boldsymbol{\Phi}^{\mathrm{T}}\,\tilde{\boldsymbol{\omega}}\,\mathbf{J}\,\mathbf{u}\,\mathrm{d}v - \int_{vol}\rho\boldsymbol{\Phi}^{\mathrm{T}}\,\tilde{\dot{\boldsymbol{\omega}}}\,\mathbf{u}\,\mathrm{d}v$$
$$+\int_{vol}\rho\boldsymbol{\Phi}^{\mathrm{T}}\,\tilde{\boldsymbol{\omega}}^{\mathrm{T}}\,\tilde{\boldsymbol{\omega}}\,\mathbf{u}\,\mathrm{d}v - \int_{vol}\rho\boldsymbol{\Phi}^{\mathrm{T}}\,\mathrm{d}v\,\mathbf{T}^{\mathbf{T}}\,\ddot{\mathbf{p}}_0 + \mathbf{Q}$$

The modal properties are computed from a finite element (FE) model, therefore it is adequate to use the FE methodology for computing the equation of motion numerically. The mode shape functions are obtained into the *e*-th element of the FE mesh as follows:

$$\boldsymbol{\Phi}(\mathbf{u}) = \mathbf{N}^e(\mathbf{u})\boldsymbol{\Phi}^e_{FE}, \tag{11}$$

where $\mathbf{N}^e(\mathbf{u})$ is the basis (or shape) function matrix of the *e*-th element, and $\boldsymbol{\Phi}^e_{\mathrm{FE}}$ the mode shapes computed in the nodes of the *e*-th element through the FE model.

This approach allows obtaining the matrices of the equation of motion by means of the matrices of the elements. These matrices have to be assembled in global matrices by following the standard FE assembling technique. The first matrix in Eq. (10) is obtained by means of the approach in Eq. (11) as follows:

$$\begin{aligned}\widetilde{\mathbf{V}} &= \int_{vol} \rho \boldsymbol{\Phi}^{\mathrm{T}} \left(\sum_i \widetilde{u}_i \frac{\partial \boldsymbol{\Phi}}{\partial u_i} \right) \mathrm{d}v = \sum_{e=1}^{n_e} \int_{vol^e} \rho \boldsymbol{\Phi}_{\mathrm{FE}}^{e\ \mathrm{T}} \mathbf{N}^{e\mathrm{T}} \left(\sum_i \widetilde{u}_i \frac{\partial \mathbf{N}^e}{\partial u_i} \right) \boldsymbol{\Phi}_{\mathrm{FE}}^e \, \mathrm{d}v \\ &= \boldsymbol{\Phi}_{\mathrm{FE}}^{\mathrm{T}} \left(\sum_{e=1}^{n_e} \int_{vol^e} \rho \mathbf{N}^{e\mathrm{T}} \left(\sum_i \widetilde{u}_i \frac{\partial \mathbf{N}^e}{\partial u_i} \right) \mathrm{d}v \right) \boldsymbol{\Phi}_{\mathrm{FE}}\end{aligned}, \tag{12}$$

being defined $\mathbf{V}^e$ as the corresponding matrix of the *e*-th element, that is:

$$\mathbf{V}^e = \int_{vol^e} \rho \mathbf{N}^{e\mathrm{T}} \left(\sum_i \widetilde{u}_i \frac{\partial \mathbf{N}^e}{\partial u_i} \right) \mathrm{d}v \,,\ \widetilde{\mathbf{V}} = \boldsymbol{\Phi}_{\mathrm{FE}}^{\mathrm{T}} \left(\sum_{e=1}^{n_e} \mathbf{V}^e \right) \boldsymbol{\Phi}_{\mathrm{FE}} \,, \tag{13}$$

where n_e is the number of elements in the FE mesh, vol is the volume domain associated with the undeformed solid, and vol^e is the volume of the *e*-th element. Following the same procedure as in Eq. (12), the remaining matrices of the equation of motion are obtained:

$$\mathbf{P}^e = \int_{vol^e} \rho \mathbf{N}^{e\mathrm{T}} \widetilde{\boldsymbol{\omega}} \mathbf{N}^e \, \mathrm{d}v \,,\ \widetilde{\mathbf{P}} = \boldsymbol{\Phi}_{\mathrm{FE}}^{\mathrm{T}} \left(\sum_{e=1}^{n_e} \mathbf{P}^e \right) \boldsymbol{\Phi}_{\mathrm{FE}} \,, \tag{14}$$

$$\mathbf{A}^e = \int_{vol^e} \rho \mathbf{N}^{e\mathrm{T}} \left(\sum_i \sum_j \widetilde{u}_i \widetilde{u}_j \frac{\partial^2 \mathbf{N}^e}{\partial u_i \partial u_j} \right) \mathrm{d}v \,,\ \widetilde{\mathbf{A}} = \boldsymbol{\Phi}_{\mathrm{FE}}^{\mathrm{T}} \left(\sum_{e=1}^{n_e} \mathbf{A}^e \right) \boldsymbol{\Phi}_{\mathrm{FE}} \,, \tag{15}$$

$$\mathbf{C}^e = \int_{vol^e} \rho \mathbf{N}^{e\mathrm{T}} \left(\sum_{i=1,3} u_i \frac{\partial \mathbf{N}^e}{\partial u_i} \right) \mathrm{d}v \,,\ \widetilde{\mathbf{C}} = \boldsymbol{\Phi}_{\mathrm{FE}}^{\mathrm{T}} \left(\sum_{e=1}^{n_e} \mathbf{C}^e \right) \boldsymbol{\Phi}_{\mathrm{FE}} \,, \tag{16}$$

$$\mathbf{S}^e = \int_{vol^e} \rho \mathbf{N}^{e\mathrm{T}} \widetilde{\boldsymbol{\omega}} \left(\sum_i \widetilde{u}_i \frac{\partial \mathbf{N}^e}{\partial u_i} \right) \mathrm{d}v \,,\ \widetilde{\mathbf{S}} = \boldsymbol{\Phi}_{\mathrm{FE}}^{\mathrm{T}} \left(\sum_{e=1}^{n_e} \mathbf{S}^e \right) \boldsymbol{\Phi}_{\mathrm{FE}} \,, \tag{17}$$

$$\mathbf{R}^e = \int_{vol^e} \rho \mathbf{N}^{e\mathrm{T}} \widetilde{\dot{\boldsymbol{\omega}}} \mathbf{N}^e \, \mathrm{d}v \,,\ \widetilde{\mathbf{R}} = \boldsymbol{\Phi}_{\mathrm{FE}}^{\mathrm{T}} \left(\sum_{e=1}^{n_e} \mathbf{R}^e \right) \boldsymbol{\Phi}_{\mathrm{FE}} \,, \tag{18}$$

$$\mathbf{B}^e = \int_{vol^e} \rho \mathbf{N}^{e\mathrm{T}} \widetilde{\boldsymbol{\omega}}^{\mathrm{T}} \widetilde{\boldsymbol{\omega}} \mathbf{N}^e \, \mathrm{d}v \,,\ \widetilde{\mathbf{B}} = \boldsymbol{\Phi}_{\mathrm{FE}}^{\mathrm{T}} \left(\sum_{e=1}^{n_e} \mathbf{B}^e \right) \boldsymbol{\Phi}_{\mathrm{FE}} \,, \tag{19}$$

$$\mathbf{c}^e = \int_{vol^e} \rho \mathbf{N}^{e\mathrm{T}} \mathbf{E} \mathbf{u} \, \mathrm{d}v \,,\ \widetilde{\mathbf{c}} = \boldsymbol{\Phi}_{\mathrm{FE}}^{\mathrm{T}} \left(\sum_{e=1}^{n_e} \mathbf{c}^e \right), \tag{20}$$

$$\mathbf{U}^e = \int_{vol^e} \rho \mathbf{N}^{e\mathrm{T}} \widetilde{\boldsymbol{\omega}} \mathbf{J} \mathbf{u} \, \mathrm{d}v \,,\ \widetilde{\mathbf{U}} = \boldsymbol{\Phi}_{\mathrm{FE}}^{\mathrm{T}} \left(\sum_{e=1}^{n_e} \mathbf{U}^e \right), \tag{21}$$

$$\mathbf{H}^e = \int_{vol^e} \rho \mathbf{N}^{e\mathrm{T}} \widetilde{\dot{\boldsymbol{\omega}}} \mathbf{u} \, \mathrm{d}v \,,\ \widetilde{\mathbf{H}} = \boldsymbol{\Phi}_{\mathrm{FE}}^{\mathrm{T}} \left(\sum_{e=1}^{n_e} \mathbf{H}^e \right), \tag{22}$$

$$\mathbf{N}^e = \int_{vol^e} \rho \mathbf{N}^{e\mathrm{T}} \tilde{\boldsymbol{\omega}}^{\mathrm{T}} \tilde{\boldsymbol{\omega}} \mathbf{u} \, \mathrm{d}v \,, \; \tilde{\mathbf{N}} = \boldsymbol{\Phi}_{\mathrm{FE}}^{\mathrm{T}} \left(\sum_{e=1}^{n_e} \mathbf{N}^e \right), \tag{23}$$

$$\mathbf{G}^e = \int_{vol^e} \rho \mathbf{N}^{e\mathrm{T}} \, \mathrm{d}v \,, \; \tilde{\mathbf{G}} = \boldsymbol{\Phi}_{\mathrm{FE}}^{\mathrm{T}} \left(\sum_{e=1}^{n_e} \mathbf{G}^e \right) \mathbf{T}^{\mathbf{T}} \ddot{\mathbf{p}}_0 \,, \tag{24}$$

resulting the following equation of motion for the flexible wheelset running along a curved track:

$$\ddot{\mathbf{q}} + \left(2\Omega \tilde{\mathbf{V}} + 2\tilde{\mathbf{P}} \right) \dot{\mathbf{q}} + \left(\Omega^2 \left(\tilde{\mathbf{A}} - \tilde{\mathbf{C}} \right) + 2\Omega \tilde{\mathbf{S}} + \tilde{\mathbf{R}} - \tilde{\mathbf{B}} + \tilde{\mathbf{D}} \right) \mathbf{q} = \Omega^2 \tilde{\mathbf{c}} - 2\Omega \tilde{\mathbf{U}} - \tilde{\mathbf{H}} + \tilde{\mathbf{N}} - \tilde{\mathbf{G}} + \mathbf{Q}_c + \mathbf{Q}_s \,. \tag{25}$$

The matrices $\tilde{\mathbf{V}}$, $\tilde{\mathbf{P}}$, $\tilde{\mathbf{A}}$, $\tilde{\mathbf{C}}$, $\tilde{\mathbf{S}}$, $\tilde{\mathbf{R}}$ and $\tilde{\mathbf{B}}$ account for inertial effects associated with the deformed configuration originated by Coriolis, centrifugal and tangential acceleration of the wheelset, as produced by the track frame motion and by the rotation of the wheelset around its axis. The vectors $\tilde{\mathbf{c}}$, $\tilde{\mathbf{U}}$, $\tilde{\mathbf{H}}$, $\tilde{\mathbf{N}}$ and $\tilde{\mathbf{G}}$ account for inertial effects not depending on wheelset deformation, which are also originated by Coriolis, centrifugal and tangential acceleration experienced by the wheelset. The diagonal matrix $\tilde{\mathbf{D}}$ is the modal stiffness matrix that contains the square of the undamped natural frequencies of the free-boundary wheelset. Finally, $\mathbf{Q}_c$ and $\mathbf{Q}_s$ are the vectors of the generalized forces acting on the flexible wheelset resulting respectively from wheel-rail contact forces, see Section 4, and from the forces applied by the primary suspension, see Section 2.2.

2.2. Boundary conditions

While running through a curve, the wheelset develops steady-state values of the creepages and contact forces that are substantially different from the case of tangent track running. On account of the non-linearity of wheel-rail contact, these steady-state contact forces and creepages strongly affect the coupled dynamics of the wheelset and of the track in the entire frequency range addressed in this paper, and therefore need to be properly taken into account in the numerical simulation procedure.

To this aim, the flexible wheelset model introduced in 2.1 is subjected to appropriate boundary conditions that are obtained from a simulation of the low frequency running dynamics of the complete vehicle along the curve considered. The low frequency simulation is performed using a multi-body model of the vehicle defined in software ADTreS developed at Politecnico di Milano [12] and considers the carbody, two bogies and four wheelsets all modelled as rigid bodies. Given that the interest of the rigid body simulation is only to derive the steady-state curving condition for the vehicle, no effect of track irregularity or wheel imperfections is considered.

In order to ensure that the contact forces and creepages are correctly initialised, the steady-state forces applied on the wheelset at the axle boxes via the primary suspension along the $\mathbf{Z}_T$ and $\mathbf{Y}_T$ axes of the trajectory coordinate frame are prescribed in Eq. (25) to match the values obtained in the low-frequency simulation: in this way, the steady state $\mathbf{Z}_T$ component of the contact forces on the two wheels and the sum of the steady-state contact forces along the $\mathbf{Y}_T$ axis are correctly reproduced by the flexible wheelset - track model. Furthermore, the longitudinal stiffness of the primary suspension is introduced in Eq. (25) and the longitudinal displacements (i.e. directed along axis $\mathbf{X}_T$) of the bogie at the primary suspension are prescribed to match the values obtained from the low-frequency simulation. By doing so, the steady-state longitudinal and lateral creep forces on both wheels are correctly initialised in the high-frequency model. As shown in Section 5, cf. comments to Table 2, this procedure allows to obtain a very good agreement of the steady state forces for the rigid body model of the complete vehicle and for the model of the single flexible wheelset.

All the above described boundary conditions are applied on the flexible wheelset model Eq. (25) by appropriately setting the terms in vector $\mathbf{Q}_s$. These consist of the generalised forces associated with the modal coordinates $\mathbf{q}$ of the concentrated forces applied at the axle-box seats, defined as explained above in this section.

3. THE TRACK MODEL

The track model has been adapted from the one presented in reference [13] where cyclic boundary conditions were adopted. With respect to this previous work, here different sleeper bay distances have been considered in order to take into account the dynamics of a constant radius curved track.

The cyclic track approach that is used in the present paper models a circumferential constant radius track negotiated by a set of identical vehicles, uniformly distributed in such a way that each vehicle is set at a constant distance L apart from the adjacent ones and travel at the same velocity V, see Figure 2. The constant distance L is set large enough to avoid the dynamic interaction between the vehicles and cyclic boundary conditions are introduced at the ends of the model. Hence, due to the periodicity of the structure and of the loading conditions, the study of the track is reduced to a single section having finite length L.

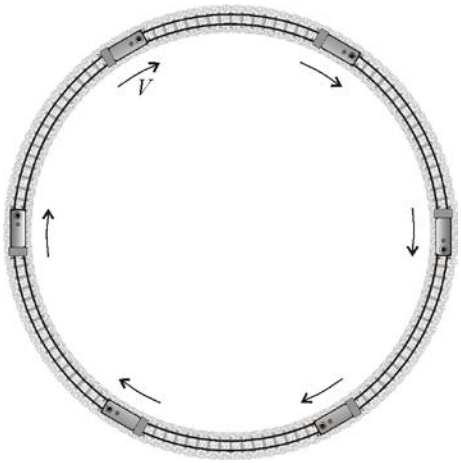

Figure 2: The cyclic track model.

The approach adopts a substructuring technique where rails and sleepers are treated separately. The rails are modelled as Timoshenko beams, including bending deformations in vertical/lateral directions, as well as torsional deformations. Rail vibration is introduced in terms of modal superposition for the unconstrained rail with cyclic boundary conditions, hence resulting into a set of de-coupled 1-d.o.f. equations.

The discrete rail supports are introduced in the form of lumped parameter systems. The rail pads are modelled as lumped visco-elastic elements generating the interaction forces between the rails and the sleepers, represented as lumped masses. Ballast dynamics is neglected here, being not relevant for the dynamic behaviour of the wheelset, but the equivalent ballast stiffness and damping are accounted for by means of lumped spring and dashpot elements.

The lateral and vertical displacements of the rail axis are [13]:

$$w^y(x,t) = \sum_r W_r^y(x)\, q_r^y(t), \tag{26}$$

$$w^z(x,t) = \sum_r W_r^z(x)\, q_r^z(t), \tag{27}$$

and the torsion and the rotations of the rail's cross-section are:

$$\psi^x(x,t) = \sum_r \Psi_r^x(x)\, q_r^x(t), \tag{28}$$

$$\psi^y(x,t) = \sum_r \Psi_r^y(x)\, q_r^z(t), \tag{29}$$

$$\psi^z(x,t) = \sum_r \Psi_r^z(x)\, q_r^y(t), \tag{30}$$

where $W_r^y(x)$, $W_r^z(x)$, $\Psi_r^x(x)$, $\Psi_r^y(x)$ and $\Psi_r^z(x)$ are the r-th modal functions of the Timoshenko periodic beam, and $q_r^x(t)$, $q_r^y(t)$ and $q_r^z(t)$ are the modal coordinates associated with torsional, lateral and vertical rail vibrations, respectively.

The resulting equations of motion for the cyclic track model in modal coordinates take the form:

$$\ddot{q}_r + 2\,\xi_r\,\omega_r\,\dot{q}_r + \omega_r^2\,q_r = f_r, \tag{31}$$

being ω_r the r-th undamped frequency and ξ_r is the modal damping. The modal forces f_r are computed from the wheel rail contact forces acting on the track.

In this way, the displacements of the rail in the present contact point can be evaluated from the displacements and rotations of the rail axis as follows:

$$\mathbf{x}_{r,j} = \mathbf{E}_j \left(w_j^y \quad w_j^z \quad \psi_j^x \quad \psi_j^y \quad \psi_j^z \right)^{\mathrm{T}}, \tag{32}$$

where $\mathbf{x}_{r,j}$ is the vector of contact point displacements in j-th rail, and the matrix $\mathbf{E}_j$ relates the displacements in rail axis and contact points.

4. THE MODEL OF THE WHEEL-RAIL CONTACT FORCES

Equations (25) and (31) are coupled by the wheel-rail contact forces, which can be defined as function of the wheelset modal coordinates $\mathbf{q}$ and their time derivatives $\dot{\mathbf{q}}$ and of the track displacements $\mathbf{x}_r$ together with their time derivatives $\dot{\mathbf{x}}_r$. The calculation of the contact forces is performed within the time step integration of the equations of motion for the wheelset and the track. First the motion (position and speed) of the contact points on wheel and rail surfaces is determined, then the normal and tangential wheel-rail contact forces are computed as a function of the relative wheel-rail motion at the contact point, finally the generalised forces on the vehicle and track coordinates are defined based on the principle of virtual work.

4.1 Contact kinematics

Using the modal superposition principle, the vectors $\mathbf{r}_{w,j}$ of the wheel displacements at the contact point (with j = 1,2 representing the left and right wheel) are computed as:

Commentato [LB1]: This is an ordinary modal approach. Please, consider to sum it up.

Commentato [S.B.2]: I suggest we keep this subsection a sit is now, and sum it up in case this is required by the reviewers.

$$\mathbf{r}_{w,j} = \mathbf{\Phi}\left(\mathbf{u}_{w,j}\right)\mathbf{q}(t) + \mathbf{r}_{w,j}^{(irr)}(t), \tag{33}$$

with $\mathbf{u}_{w,j}$ the position of the contact point on the wheel and $\mathbf{r}_{w,j}^{(irr)}$ a vector accounting for the effect of wheel out-of-roundness, which is defined as a periodical function of time. In the same way, the "material velocity" vectors $\dot{\mathbf{r}}_{w,j}^{(M)}$ of the wheel at the contact point, i.e. the velocity of the material point on each wheel instantaneously in contact with the rail are defined as:

$$\dot{\mathbf{r}}_{w,j}^{(M)} = \mathbf{\Phi}\left(\mathbf{u}_{w,j}\right)\dot{\mathbf{q}}(t) + \Omega\left(\sum_i \tilde{u}_i \frac{\partial \mathbf{\Phi}}{\partial u_i}\right)\mathbf{q}(t). \tag{34}$$

The rail displacements at the contact points on the left and right rails $\mathbf{r}_{r,j}$ are obtained according to the following expression:

$$\mathbf{r}_{r,j} = \mathbf{x}_{r,j}(t) + \mathbf{r}_{r,j}^{(irr)}(t), \tag{35}$$where

$\mathbf{r}_{r,j}^{(irr)}$ is a vector accounting for the effect of geometric imperfections in the track due to irregularity and rail roughness, whereas the material velocity of the rails at the contact points is computed as:

$$\dot{\mathbf{r}}_{r,j}^{(M)} = \dot{\mathbf{x}}_{r,j}^{(M)} = \mathbf{E}_j \begin{pmatrix} \dot{w}_j^y & \dot{w}_j^z & \dot{\psi}_j^x & \dot{\psi}_j^y & \dot{\psi}_j^z \end{pmatrix}^{\mathrm{T}} + V\,\mathbf{E}_j \frac{\partial}{\partial x}\begin{pmatrix} w_j^y & w_j^z & \psi_j^x & \psi_j^y & \psi_j^z \end{pmatrix}^{\mathrm{T}}. \tag{36}$$

being *V* the speed of the wheelset.

4.2 Calculation of wheel-rail contact forces

The model of wheel-rail contact used to reproduce the dynamic coupling between the vehicle and the track is a pre-tabulated, multi-Hertzian one [14]. Prior to the simulation, wheel-rail contact geometry is processed starting from measured or theoretical wheel and rail profiles and the contact parameters required to compute wheel-rail contact forces are stored in a contact table. These include the contact angle, the variation of the wheel rolling radius with respect to the nominal one, the curvatures of the wheel and rail profiles in the contact point region and an undeformed distance which is equal to zero for the geometric contact point and greater than zero for the other potential contact points. More details on the process used to derive the contact table can be found in [15], note that with respect to the theory presented there, in this work the effect of the angle of attack is neglected, thus leading to a simplified planar contact problem.

In order to compute the contact forces at time *t*, the relative wheel – rail lateral displacement is computed and the contact tables are interpolated, finding the contact parameters for one or more wheel-rail potential contact points. Then, for each *i*-th potential contact point of the *j*-th wheel-rail couple the so-called "normal problem" is solved. To this aim, an elastic inter-penetration is computed by projecting the relative wheel-rail displacements in the contact point along the direction normal to the contact plane, which is defined by the contact angle parameter in the contact table. To consider the change with time of the normal direction, the inter-penetration is computed according to an incremental definition, so that the penetration $p_{i,j}^{(t)}$ at time t is defined as the sum of the penetration at the previous time step *t-Δt* plus the penetration increment from the previous to the present time step:

$$p_{i,j}^{(t)} = p_{i,j}^{(t-\Delta t)} + \mathbf{n}_i^T\left(\left(\mathbf{r}_{w,j}^{(t)} - \mathbf{r}_{w,j}^{(t-\Delta t)}\right) - \left(\mathbf{r}_{r,j}^{(t)} - \mathbf{r}_{r,j}^{(t-\Delta t)}\right)\right) - \left(\delta_{i,j}^{(t)} - \delta_{i,j}^{(t-\Delta t)}\right), \tag{37}$$

where $\mathbf{n}_i$ is the vector defining the normal direction for the *i*-th contact, $\delta_{i,j}$ is the undeformed distance for the *i*-th contact of the *j*-th wheel-rail couple, and superscripts "*(t)*" and "*(t-Δt)*" denote quantities evaluated at the present and previous time step respectively.

The normal force $N_{i,j}^{(t)}$ is computed as function of the elastic inter-penetration according to Hertz's formulae using the profile curvatures retrieved from the contact table:

$$\begin{cases} N_{i,j}^{(t)} = 0 & \text{if} \quad p_{i,j}^{(t)} \le 0 \\ N_{i,j}^{(t)} = C_{i,j}\left(p_{i,j}^{(t)}\right)^{\frac{3}{2}} & \text{if} \quad p_{i,j}^{(t)} > 0 \end{cases}. \tag{38}$$

The creep forces are then computed as function of the creepages, according to the heuristic formulae by Shen, Hedrick & Elkins [16]. The longitudinal and transversal creepages, $\varepsilon_{L_{i,j}}$ and $\varepsilon_{T_{i,j}}$ respectively, are computed as follows:

$$\varepsilon_{L_{i,j}} = \frac{\mathbf{l}_i^T\left(\dot{\mathbf{r}}_{w,j}^{(M)} - \dot{\mathbf{r}}_{r,j}^{(M)}\right)}{V} - \frac{\Delta R_{i,j}}{R_0} + \frac{s}{R_0}(-1)^j, \tag{39}$$

$$\varepsilon_{T_{i,j}} = \frac{\mathbf{t}_i^T\left(\dot{\mathbf{r}}_{w,j}^{(M)} - \dot{\mathbf{r}}_{r,j}^{(M)}\right)}{V} -$$

with $\mathbf{l}_i$ and $\mathbf{t}_i$ the vectors defining the longitudinal and transversal direction for the *i*-th contact, V the speed of the wheelset, $\Delta R_{i,j}$ the rolling radius variation for the contact point under consideration, σ_j the angle of attack of the wheel, s half-distance between the wheel nominal running circles and γ_j the contact angle of the wheel at the actual contact point.

Finally, the normal and creep forces obtained at each *i*-th wheel-rail contact point are projected along the trajectory frame $\mathbf{X}_T\mathbf{Y}_T\mathbf{Z}_T$ and summed over all active contacts occurring in the same wheel-rail couple, and the components of the resulting contact forces along the modal coordinates $\mathbf{q}$ are derived by standard application of the principle of virtual work, providing vector $\mathbf{Q}_s$ in Eq. (25).

5. RESULTS

In this section, results of wheelset-track interaction simulations are presented considering different sources of excitation: a single harmonic rail corrugation, random rail roughness and a wheelflat. Results are also presented for a rigid wheelset model, i.e. including in the modal synthesis only the rigid modes of vibration of the unconstrained wheelset. In this way, the effect of wheelset flexibility is pointed out. Furthermore, for of the wheelflat excitation case, results are also presented for the wheelset running at the same speed in tangent track, to assess the effect of curving on high-frequency wheelset-track interaction, which is the main innovation introduced in this paper.

The case study considered here refers to the trailed car of a concentrated power train for high-speed passenger service. The vehicle is equipped with a solid axle wheelset with monobloc, light design wheels. The track considered features UIC60 rails and track parameters are based on the EUROBALT project [17], considering a "stiff" track. Table 1 summarises the input data used to set-up the simulation model.

Wheelset model data		**Track model data**	
Mass of wheelset	1375 kg	Sleeper bay	0.6 m
Axle load	120 kN	Sleeper number	70
Primary suspension longitudinal stiffness	7.5 MN/m	Sleeper mass	324 kg
Primary suspension lateral stiffness	7.1 MN/m	Track bed stiffness	200 MN/m
Primary suspension vertical stiffness	0.81 MN/m	Track bed damping	150 kNs/m

Primary suspension longitudinal damping	100 kNs/m	Rail pad stiffness	1 GN/m
Primary suspension lateral damping	100 kNs/m	Rail pad damping	50 kNs/m
Primary suspension vertical damping	30 kNs/m	Rail section	UIC60

Table 1: Simulation parameters

All simulation cases presented below consider the wheelset running at 150 km/h through a curve with radius 1000 m with cant deficiency 150 mm approximately. For this running condition, Table 2 compares the steady-state values of the contact force components for the rigid body model of the complete vehicle and for the model of the single flexible wheelset: a very good agreement of the two series of data is observed, leading to the conclusion that, at least for the considered running condition, the procedure introduce in Section 2.2 is able to correctly set-up the boundary conditions for the flexible wheelset model. Note that in Table 2 and below in this section 'vertical', 'lateral' and 'longitudinal' force respectively mean the component of the contact force along the $\mathbf{Z}_T$, $\mathbf{Y}_T$ and $\mathbf{X}_T$ axis of the track following reference.

	Outer wheel		Inner wheel	
	Rigid multi-body model	Flexible wheelset model	Rigid multi-body model	Flexible wheelset model
Vertical force	69.57 kN	70.01 kN	49.82 kN	49.71 kN
Lateral force	5,68 kN;	5,91 kN	-3,75 kN;	-3,99 kN
Longitudinal force	14.39 kN;	15.16 kN	-14.39 kN;	-15.16 kN

Table 2: Steady-state wheel-rail contact forces for the rigid multi-body model of the entire vehicle and for the single flexible wheelset model..

5.1 Results for single harmonic rail corrugation

The first excitation case considered is rail corrugation having sinusoidal waveform with wavelength 60 mm, i.e. one tenth of the sleeper bay. In Figure 3 the vertical contact force generated by the wheelset travelling on the corrugated rail at 150 km/h is plotted as a function of time. The rail roughness profile is also reported in the figure using an appropriate scaling and offset to obtain a proper visualisation.

Two harmonic contents are observed in the vertical contact force, the largest one having the same wavelength as the rail corrugation and a second one with wavelength equal to the sleeper bay. This second harmonic component is due to the periodic variation of the rail stiffness seen by the wheelset as the consequence of the discrete rail support. The contact force is also highly affected by wheelset flexibility: considering a rigid wheelset leads to an over-estimation of the peak-to-peak dynamic force by approximately 15% on the inner wheel and 40% on the outer wheel. This is due to the fact that the mass participating in the high frequency vibration of the flexible wheelset is lower than the whole mass of the wheelset, mainly due to bending deformations occurring in the axle, a mechanism which is not captured by the rigid wheelset model.

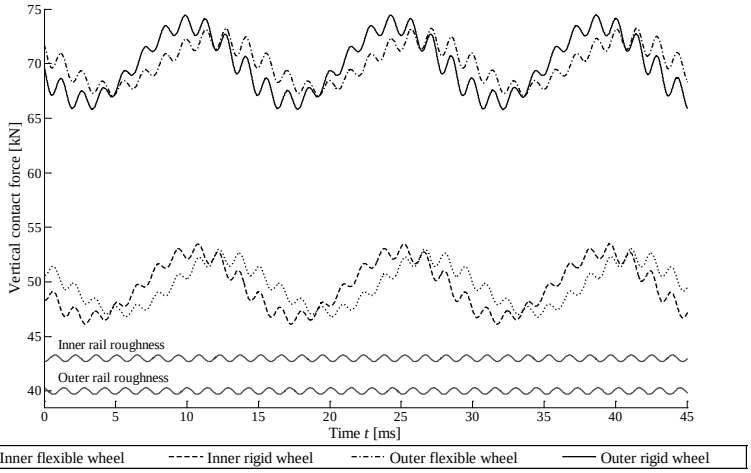

Figure 3. Vertical wheel-rail contact forces when the vehicle circulates at 150 km/h speed on a corrugated curved track (1000 m curve radius) with corrugation wavelength 60 mm. Corrugation amplitude corresponding to the ISO 3095 limit

Figure 4 shows the lateral component of the contact force on the two wheels, for the same running condition considered above. The steady state values of the contact forces (see also Table 2) reflect the curving condition of the wheelset. Here, the leading wheelset in the front bogie of the vehicle is considered, for which a small negative angle of attack takes place on account of curve negotiation, causing a steady componentof the transversal creep force which points towards the outside of the curve. This is balanced by the lateral component of the flange force on the outer wheel, leading to the typical condition of the two lateral forces pointing in opposite directions in a way that tends to widen the track gauge. Like for the vertical contact force component, the dynamic component of the lateral contact force shows two harmonic contents, one corresponding to the sleeper-passing frequency, the other corresponding to the wavelength of the harmonic corrugation introduced as the source of excitation. Also in this case, simplifying the problem to the case of a rigid wheelset leads to an over-estimation of the dynamic contact force harmonics synchronous with the corrugation. The longitudinal contact force component caused by a single harmonic rail corrugation is not shown as the level of dynamic excitation for this case is very low.

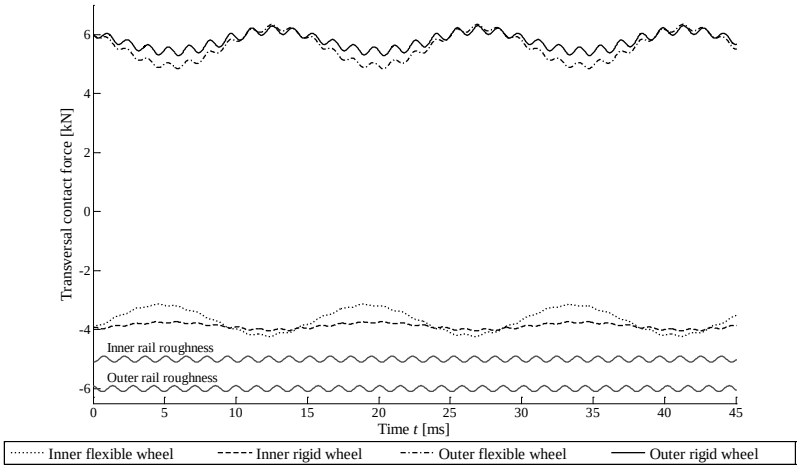

Figure 4. Lateral wheel-rail contact forces when the vehicle circulates at 150 km/h speed on a corrugated curved track (1000 m curve radius) with corrugation wavelength 60 mm. Corrugation amplitude corresponding to the ISO 3095 limit

5.2 Results for random rail corrugation

Figures 5, 6 and 7 show the time history of the vertical, lateral and longitudinal contact forces for excitation caused by randomly corrugated rails, assuming a corrugation spectrum corresponding to the ISO 3095 limit. The results obtained for a flexible and a rigid wheelset model are again compared. As expected, the dynamic fluctuations of all contact force components show a complex waveform, arising from the dynamic response of the wheelset-track system to broadband random excitation. As far as the vertical contact force component is concerned, this leads to a maximum dynamic force on the outer wheel which is 1.75 times the steady-state value in full curve, whereas on the inner wheel the minimum contact force is approximately 0.52 times the steady state value.

Compared to the results obtained using the flexible wheelset model, the use of a rigid wheelset model results in a significant over-estimation of the maximum force on the outer wheel and of the maximum wheel unloading on the inner wheel. However, for the lateral and longitudinal contact force components the situation is somehow different, as the maximum amplitude of dynamic variations for the flexible and rigid wheelset model is comparable on both the outer and inner wheels, but with important differences in the waveform of the signals.

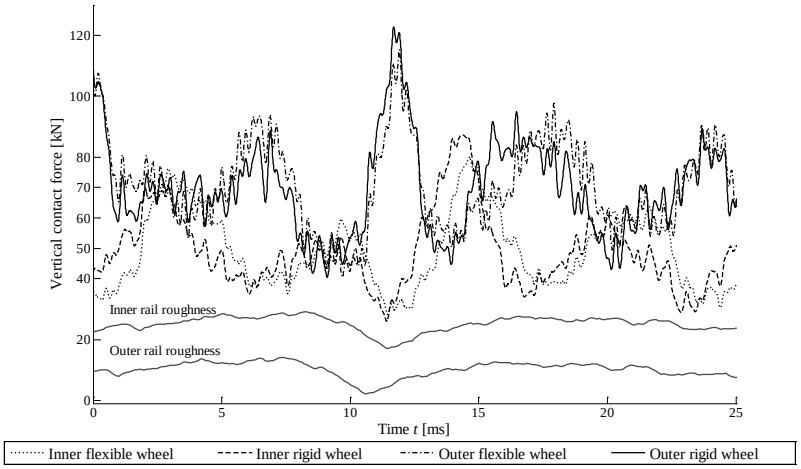

Figure 5. Vertical wheel-rail contact forces when the vehicle circulates at 150 km/h speed on a randomly corrugated curved track (1000 m curve radius). Amplitudes corresponding to the ISO 3095 limit.

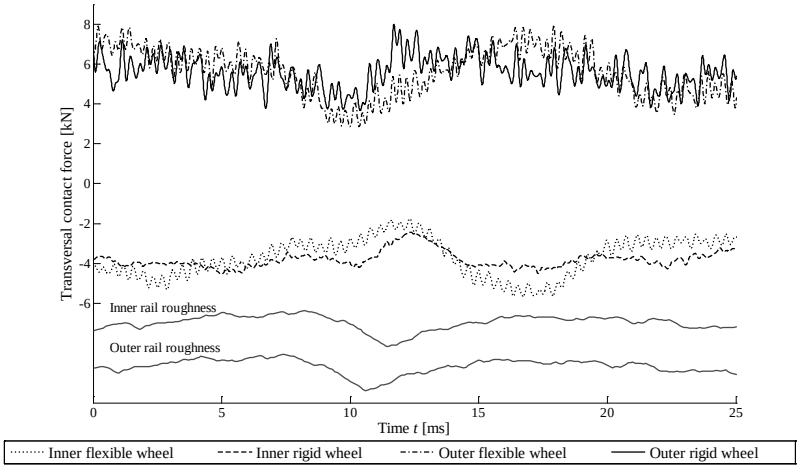

Figure 6. Lateral wheel-rail contact forces when the vehicle circulates at 150 km/h speed on a randomly corrugated curved track (1000 m curve radius). Amplitudes corresponding to the ISO 3095 limit.

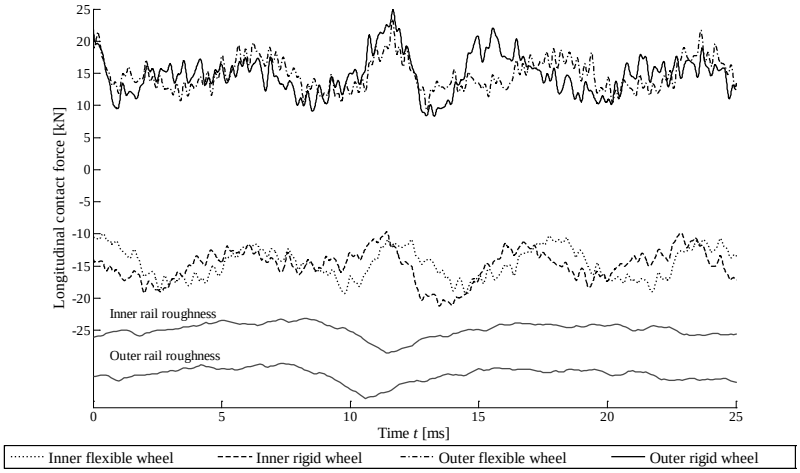

Figure 7. Longitudinal wheel-rail contact forces when the vehicle circulates at 150 km/h speed on a randomly corrugated curved track (1000 m curve radius). Amplitudes corresponding to the ISO 3095 limit.

5.3 Results for a wheel flat

Figures 8, 9 and 10 show the time history of the vertical, lateral and longitudinal contact forces caused by a wheelflat when the wheelset runs over a perfectly even track. Results are presented for the same running condition in curved track considered in 5.1 and 5.2. The wheel flat is assumed to occur on the inner and outer wheel at the same time. Intense dynamic effects are observed, initially leading to the occurrence of full loss of contact at both wheels, then followed by a severe impact causing peaks in all force components, and finally by a transient vibration that generates further dynamic fluctuations in all contact force components.

As far as the vertical contact force component is concerned, the maximum overloading on the inner wheel is 308% of the steady-state load, whereas on the outer wheel the maximum overloading reaches 362% of the steady state load. For the lateral force component (Figure 9), the peak load is much larger on the outer wheel than on the inner one, on account of the greater contact angle experienced by the outer wheel as a consequence of the lateral shift of the leading wheelset towards the outside of the curve: this is an effect that is not captured by models neglecting curving effects. Also for the longitudinal contact force component (Figure 10) the peak value is larger on the outer wheel, on account of the larger normal contact force occurring on that wheel, which generates then a larger creep force for the same or similar creepage condition.

The differences between the results for the rigid and flexible wheelset model are small in terms of duration of the contact loss and of maximum overloading in vertical direction (the rigid wheelset model over-estimates the peak vertical load on the outer wheel by 7% approximately with respect to the flexible wheelset model), but the transient following the impact is affected quite remarkably by wheelset flexibility, as demonstrated by the fluctuations of the contact force components following the impact. Furthermore, the maximum value of the lateral contact force on the outer wheel is much larger when the rigid wheelset model is used, with an increase in the range of 40%, whereas the maximum value of the longitudinal contact force is less affected by wheelset flexibility.

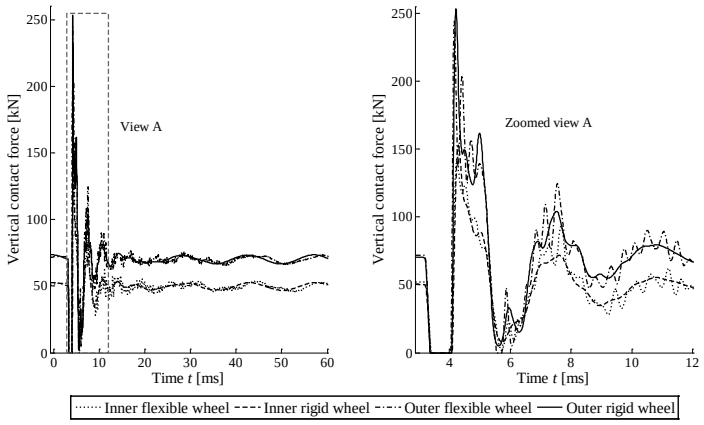

Figure 8. Vertical wheel-rail contact forces when the vehicle circulates at 150 km/h speed on a perfectly even curved track (1000 m curve radius) in presence of a 50 mm wheelflat.

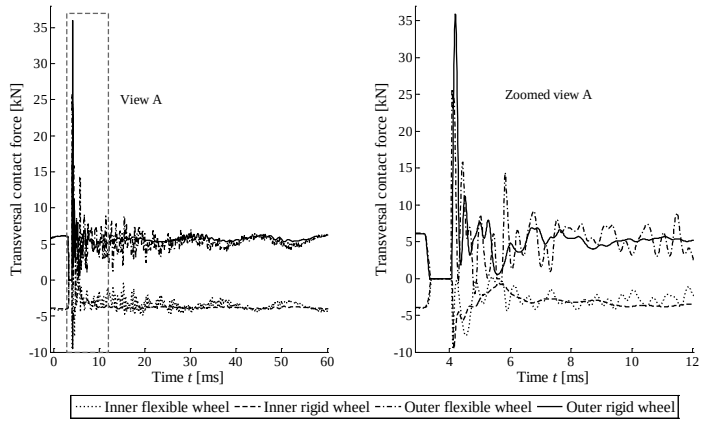

Figure 9. Lateral wheel-rail contact forces when the vehicle circulates at 150 km/h speed on a perfectly even track in presence of a 50 mm wheelflat.

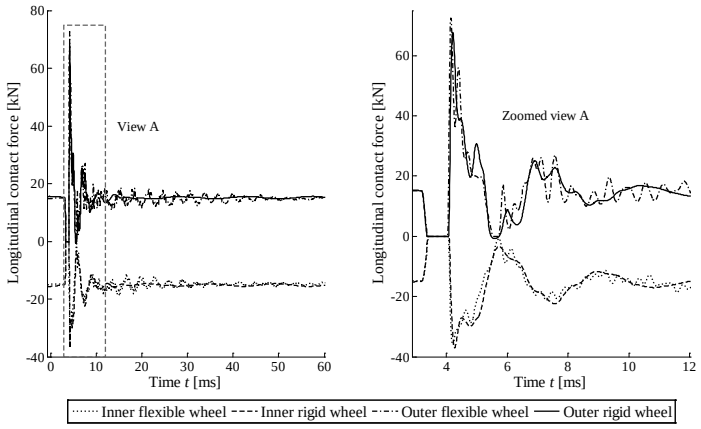

Figure 10. Longitudinal wheel-rail contact forces when the vehicle circulates at 150 km/h speed on a perfectly even track in presence of a 50 mm wheelflat.

In Figure 11 results are presented for the same wheelset excitation considering the vehicle running at the same speed (150 km/h) in tangent track. Because dynamic effects in lateral and longitudinal direction are in this case relatively modest, only the vertical force component is shown. Furthermore, because of the symmetry in the running condition considered, the forces on the two wheels are the same and therefore results are shown for one single wheelset. Apart from the difference in the steady state value of the contact forces, the waveform of the contact force time history in Figure 11 looks similar to the result obtained for curve negotiation in Figure 8. However, the peak force is approximately 180 kN, compared to 250 kN for the outer wheel in the curving condition, showing that wheelflat excitation in a curve may lead to considerable overloading of the wheelset and rails and can therefore be expected to cause accelerated damage and degradation of the contacting surfaces as well as increased noise and vibration.

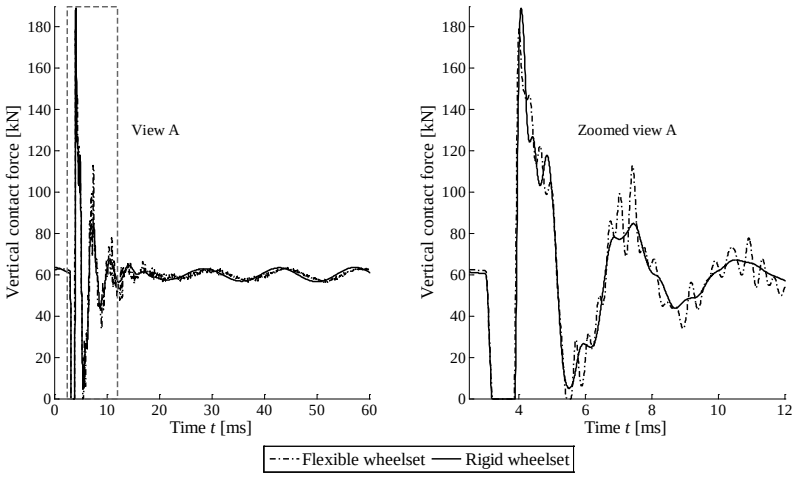

Figure 11. Vertical wheel-rail contact forces when the vehicle circulates at 150 km/h speed on a perfectly even tangent track in presence of a 50 mm wheelflat.

6. CONCLUSIONS

This paper has presented a model for a flexible wheelset running on a flexible curved track. By introducing a trajectory coordinates set describing the large motion of the wheelset along the curved track and assuming small relative movements of the wheelset with respect to the trajectory frame, the terms appearing in the wheelset equations of motion can be efficiently computed, keeping the time required to carry the numerical simulation within acceptable limits. At the same time, the model accurately describes the vibration of the flexible wheelset in the frequency range up to 2.7 kHz. The flexible wheelset is coupled to a periodic curved track model by a non-linear description of wheel-rail contact forces.

Appropriate boundary conditions are prescribed at the wheelset axle-boxes in terms of vertical and lateral forces and longitudinal displacements above the primary suspension, to correctly reproduce the steady state contact forces and creepages as obtained from a simulation of the low frequency running dynamics of the complete vehicle along the curve considered. The results reported in Table 2 show that this method succeeds in establishing the appropriate steady state contact condition on both wheels, for the exemplary curving condition considered in this paper.

Results are presented for three types of excitation: single harmonic rail corrugation, randomly corrugated track and excitation arising from a wheel flat when the wheelset runs over a perfectly even track. One exemplary curving condition was considered, which consists of the wheelset running along a 1000 m radius curve at 150 km/h and 150 mm cant deficiency. To point out the implications of modelling wheelset flexibility, results are also presented for the case of a rigid wheelset.

In all three excitation cases considered, the rigid wheelset model leads to an over-estimation of the maximum contact forces, compared to the flexible wheelset model. For the vertical contact force component, this effect is particularly significant with excitation coming from a corrugated rail (either with single harmonic or random corrugation) whereas differences between the two models

are less important in the case of wheel flat excitation. However, in case of wheel flat excitation a very large difference of the results obtained for the rigid and flexible wheelset model is observed for the lateral component of the contact force.

Finally, for the case of wheel flat excitation results obtained for the wheelset running in curve where compared to the case of the wheelset running at the same speed in tangent track: this comparison shows that the peak load in the vertical force component is approximately 39% larger when the wheelset runs in curve compared to the tangent track running case, leading to the conclusion that wheelflat excitation in a curve may lead to considerable overloading of the wheelset and rails and can therefore be expected to cause accelerated damage and degradation of the contacting surfaces as well as increased noise and vibration.

It is worth noticing that the effects of wheel flat excitation in a curve have not been extensively studied in the past, so this topic is suggested for further investigation in the future, looking e.g. at the effect of parameters such as curve radius, cant deficiency, wheel profiles, bogie and suspension design. Further use of the model presented here is also envisaged to investigate problems such as rail corrugation, squeal noise, dynamic stresses in wheels, axles and rails.

7. REFERENCES

[1] D. J. Thompson, Railway Noise and Vibration: Mechanisms, Modelling and Means of Control, Elsevier, 2009.

[2] J. C. O. Nielsen, R. Lundén, A. Johansson and T. Vernersson, Train-track Interaction and Mechanisms of Irregular Wear on Wheel and Rail Surfaces, Vehicle System Dynamics (2003) 40 (1-3), 3-54.

[3] A. Ekberg, Fatigue of railway wheels, In: The Wheel/Rail Interface Handbook Woodhead Publishing in Mechanical Engineering, Pages: 211-244, 2009.

[4] S.L. Grassie, R.W. Gregory, D. Harrison, K. L. Johnson, Dynamic response of railway track to high frequency vertical excitation, Journal of Mechanical Engineering Science 24 (1982) 77-90

[5] G. Diana, F. Cheli, S. Bruni, A. Collina, Experimental and numerical investigation on subway short pitch corrugation, Vehicle System Dynamics (1998) 29 (Suppl.), 234-245.

[6] A. Johansson, Out-of-round railway wheels – causes and consequences: an investigation including field tests, out-of-roundness measurements and numerical simulations, Doctoral dissertation, Chalmers University, September 2005.

[7] K. Popp and I. Kaiser, Interaction of elastic wheelsets and elastic rails: modelling and simulation, Vehicle System Dynamics (2006) 44 (Suppl.), 932-939.

[8] D. J. Thompson and C. J. C. Jones, A Review of the Modelling of Wheel/Rail Noise Generation, Journal of Sound and Vibration (2000) 231(3), 519-536.

[9] I. Kaiser, Refining the modelling of vehicle-track interaction, Vehicle System Dynamics (2012) 50 (SI), 229-243.

[10] L. Baeza, J. Fayos, A. Roda and R. Insa, High frequency railway vehicle-track dynamics through flexible rotating wheelsets, Vehicle System Dynamics (2008) 46 (7) 647 – 662.

[11] P. T. Torstensson, J. C. O. Nielsen and L. Baeza, Dynamic train-track interaction at high vehicle speeds-Modelling of wheelset dynamics and wheel rotation, Journal of Sound and Vibration 330 (2011), 5309-5321.

[12] S. Bruni, A. Collina, G. Diana, P. Vanolo, Lateral dynamics of a railway vehicle in tangent track and curve: tests and simulation, Vehicle System Dynamics (2000) 33 (Suppl.) 464-477.

[13] L. Baeza, H. Ouyang, A railway track dynamics model based on modal substructuring and a cyclic boundary condition, Journal of Sound and Vibration 330 (2011) 75–86.

[14] J. Piotrowski, H. Chollet, Wheel-rail contact models for vehicle system dynamics including multi-point contact, Vehicle System Dynamics, 43 (6), 455-483. 2005.

[15] F. Braghin, S. Bruni, G. Diana, Experimental and numerical investigation on the derailment of a railway wheelset with solid axle, Vehicle System Dynamics (2006) 44 (4), 305 – 325.

[16] Z. Y. Shen, J. K. Hedrick and J. A.Elkins, A comparison of alternative creep force models for rail vehicle dynamic analysis, Vehicle System Dynamics, (1983) 12 (Suppl.) 79 – 82.

[17] L. Mazzola, Y. Bezin, S. Bruni, Vehicle – Track interaction: MB simulation for track loading limits and damage identification ECCOMAS Thematic Conference Multibody Dynamics 2011, July 4-7 2011, Bruxelles, Belgium.